Deformation Behavior across the Zircon-Scheelite Phase Transition

Binbin Yue, Fang Hong, Sébastien Merkel, Dayong Tan, Jinyuan Yan, Bin Chen, and Ho-Kwang Mao

Phys. Rev. Lett. **117**, 135701 — Published 21 September 2016

DOI: 10.1103/PhysRevLett.117.135701

Deformation Behavior across the Zircon-Scheelite Phase Transition

Binbin Yue[1, 2], Fang Hong[1, 2*], Sébastien Merkel[3, 4*], Dayong Tan[1, 5], Jinyuan Yan[2], Bin Chen[1*], Ho-Kwang Mao[1]

[1] *Center for High Pressure Science and Technology Advanced Research, 1690 Cailun Rd, Pudong, Shanghai 201203, China*

[2]*Advanced Light Source, Lawrence Berkeley National Laboratory, Berkeley, CA 94720, USA*

[3]*Unité Matériauxet Transformations, ENSCL, CNRS, Université de Lille, 59000 Lille, France*

[4]*Institut Universitaire de France, 75005 Paris, France*

[5]*Key Laboratory of Mineralogy and Metallogeny, Guangzhou Institute of Geochemistry, Chinese Academy of Sciences, Guangzhou 510640, China*

*Corresponding email: hongfang@hpstar.ac.cn; sebastien.merkel@univ-lille1.fr; chenbin@hpstar.ac.cn.

ABSTRACT

Pressure effects on plastic deformation and phase transformation mechanisms of materials are of great importance to both Earth science and technological applications. Zircon-type materials are abundant both in nature and industrial field, however, there is still no *in situ* study on their deformation behavior. Here, by employing radial x-ray diffraction in a diamond anvil cell, we investigated the dislocation induced texture evolution of zircon-type gadolinium vanadate ($GdVO_4$) *in situ* under pressure and across its phase transitions to its high pressure polymorphs. Zircon-type $GdVO_4$ develops a (001) compression texture associated with dominant slip along <100>{001} starting from 5 GPa. This (001) texture transforms into a (110) texture during the zircon-scheelite phase transition. Our observation demonstrates a martensitic mechanism for the zircon-scheelite transformation. This work will help to understand the local deformation history in upper mantle and transition zone, and provides fundamental guidance on material design and processing for zircon-type materials.

Zircon ($ZrSiO_4$) is an ubiquitous accessory mineral in nature which can be found in a wide variety of sedimentary, igneous, and metamorphic rocks [1]. Its high-pressure polymorph, reidite with the scheelite-type structure, has also been discovered in terrestrial impact craters [2]. The ability to retain substantial chemical and isotopic information of zircon has made it useful in a wide range of geochemical investigations, from studies on the chemical evolution of Earth's crust and mantle to age dating [3,4]. During its history, zircon can be subject to plastic deformation, either through geodynamical processes [5] or shock metamorphism [6]. As such, remains of plastic deformation in zircon grains are used as a marker for deformation or records of impact in the Earth's history. Hence, the plastic deformation of zircon and its high pressure polymorphs is of general interest to the Earth science community.

In fact, there are many minerals or materials with the zircon-type structure. The orthovanadates (AVO_4) are such examples. They are a group of materials with promising optical, chemical and mechanical properties, which make them interesting for application in devices such as lasers, scintillators, and also catalysts and phosphors [7-10]. Due to the technological importance of zircon-type orthovanadates, besides their electronic and optical properties, their mechanical properties are also of interest in several areas of materials research [11]. Previous studies on orthovanadates including x-ray diffraction [12-16], Raman scattering [17] , theoretical calculations [18,19] and combined methods [20,21] show that many AVO_4 compounds with the zircon type phase transform to a scheelite-type structure (space group: $I4_1/a$) under high pressure irreversibly. However, while multiple studies focused on pressure-induced structure changes in orthovanadates, there are few reports on their plastic behavior and orientation relationships between the

low and high pressure phases. Such information is critical for the design of advanced materials, such as shape-memory alloys that rely on martensitic transformations to recover their original shape after the application of external loading conditions [22,23].

Considering the importance of zircon type materials for geology and material science, it is necessary to study their deformation behavior under high pressure. There are already some reports about the slip system of zircon-type materials during plastic deformation [5,24-27]. However, the deformation mechanism of the zircon phase under pressure is still controversial. A transmission electron microscopy (TEM) study of shock deformed zircon suggested a dominant system of <100>{010} [25]. while an electron backscatter diffraction (EBSD) investigation of natural zircon lead to dominant slips along <010>{001}, <010>{100} and <001>{010} [5]. Dislocation structures in single crystal of yttrium orthovanadate has also been identified by TEM with vector 1/2[111] and (11-2) as a possible slip plane [24]. Hence, further investigation on the deformation mechanism of zircon is still needed to address this controversy.

Here, by taking the advantage of radial x-ray diffraction technique in the diamond anvil cell (DAC) [28-32], we *in situ* investigate the deformation behavior of zircon type material $GdVO_4$ across the zircon-scheelite phase transition under high pressure up to 38 GPa. Unlike in conventional axial geometry, x-ray is sent through the x-ray transparent boron-kapton gasket and sample polycrystals perpendicular with the compression direction in radial diffraction [33]. A small fragment of ~10 μm thick platinum foil was added on top of the sample and was used as a pressure calibrate in each experiment, using the equation of state (EOS) for Pt [34]. In order to maximize the deviatoric stress on the samples, no pressure medium was used. Under the non-hydrostatic condition, the

pressure uncertainty increases with pressure and the pressure error is ± 2 GPa at 25.6 GPa. The samples were compressed between diamond culets of 300 μm diameter. The *in situ* radial x-ray diffraction and DAC deformation experiment was performed at beamline 12.2.2 of the Advanced Light Source at Lawrence Berkeley National Laboratory. A panoramic-type diamond anvil cell with large openings was used to allow radial x-ray diffraction. A monochromatic x-ray of wavelength 0.4959 Å was collimated to a beam size of 20μm×20μm and focused onto the sample. A Mar345 image plate was used to record the diffraction rings of the samples. Instrument parameters, such as sample-to-detector distance, beam center, and detector tilt, were calibrated using a LaB_6 standard prior to the experiment. Diffraction data were analyzed by the Rietveld refinement method [35] as implemented in the software package *MAUD* [36]. Lattice parameters, lattice strain and preferred orientations of both zircon and scheelite structures were extracted from the refinement results.

At ambient condition, $GdVO_4$ is in the form of zircon-type tetragonal structure with space group $I4_1/amd$, as seen in Fig.1 (a). Under high pressure, the zircon-type structure transforms to a scheelite-type tetragonal phase with space group $I4_1/a$ at 5.0 GPa. The zircon-type phase and scheelite-type phase coexist in a wide pressure range up to 23.0 GPa. With further pressure increase, a monoclinic *M*-fergusonite (*M*f) (space group: *I*2/*a*) phase appears above 31.2 GPa. However, a full conversion to the *M*f phase was not achieved in the current experiment. Therefore, the deformation behavior of the third phase will not be discussed in this work. The atomic structures of these two high pressure polymorphs are given in Fig. 1(b-c). After decompression, the quenched sample shows a pure scheelite structure, indicating that the transformation to the *M*f phase is reversible,

unlike that of zircon to scheelite structures which is non-reversible. This observation is in good agreement with the irreversible changes detected in Raman and luminescence measurements [17]. This phenomenon has also been reported in high pressure studies of natural zircon [37] and other AVO_4 materials like $TbVO_4$, $EuVO_4$, $LuVO_4$ and $ScVO_4$ [12,15]. There is also rare case in which the phase transition doesn't follow this trend. Zircon type $Tb_{0.5}Gd_{0.5}PO_4$ transformed to monazite through an intermediate anhydrite-type structure, showing a different phase transition sequence for zircon type materials under high pressure [38].

One fitting example was shown in Fig. 1(d) at 11.0 GPa where both zircon-type phase and scheelite-type phase present. More information concerning the refinement of patterns for different phases can be found in Fig. S1 and S2 of the Supplementary Material [39]. Volume fractions and hydrostatic lattice parameters of zircon, scheelite and *M*f phases of $GdVO_4$ were obtained from the refinement [39] and plotted in Fig. 2. The onset pressure of the zircon-scheelite phase transformation for $GdVO_4$ in our work is 5 GPa, which is lower than the 7 GPa reported using Raman measurements [17]. Do note, however, that a 4:1 methanol-ethanol mixture was used as pressure transmitting medium in the previous study, while we did not use any in our study. Such effect of non-hydrostatic conditions on transition pressure is well known in high pressure experiments [47,48]. The unit-cell parameters and volumes for the zircon and scheelite phases of $GdVO_4$ under pressure are summarized in Fig.2 (b-c). The volumes as a function of pressure have been fitted using 3rd-order Birch-Murnaghan EOS for both phases [39]. The *c*/*a* ratio was plotted as a function of pressure in Fig. S3 [39]. We observe a decrease of about 10.6% in volume for the zircon to scheelite phase transformation.

Figure 2 (d) displays *t*/G as a function of pressure for the zircon and scheelite phases. The stress state in a polycrystalline sample under uniaxial compression in the diamond anvil cell can be described by a maximum stress along the cell loading axis, σ_3, and a minimum stress in the radial direction, σ_1. The difference between σ_3 and σ_1 is termed the differential stress *t*. According to the lattice strains theory developed by Singh *et al*. [49], we have *t*/*G* equals to 6 times of $<Q(hkl)>$, where $<Q(hkl)>$ represents the average lattice strain value over all observed reflections, and *G* is the aggregate shear modulus of the polycrystalline sample. The *t*/*G* ratio can be readily extracted from the diffraction data and is most appropriate for comparing different materials. Such model does not account for intra-granular plastic relaxation [50]. It has been shown, however, that could be used for a first evaluation of the stress level in plastically deforming aggregates [51]. In order to extract *t*/*G* with MAUD, we used the Triaxial Stress Isotropic E strain model to refine a first value of differential stress *t* using the Young's modulus *E* and Poisson ratios *v* of $GdVO_4$ at ambient condition, from which we calculated $t/G=2t(1+v)/E$, which is independent of the choice of *E* and *v*.

For the zircon phase, *t*/G first increases from 0 at 1 atm to 0.0412 at 5 GPa. With the appearance of the scheelite phase, this value begins to decrease gradually and reaches 0.006 at 21 GPa. For the scheelite phase, the initial value is 0.036 at 5 GPa; it increases to 0.096 at 25.6 GPa. The lattice strains of the zircon phase first increase with increasing pressure. They then decrease with the appearance of the second phase. This may imply that the grains with higher deviatoric strains transform to the scheelite phase earlier, in agreement with the lower phase transformation pressure observed in our non-hydrostatic experiment. A displacive mechanism has been reported for the zircon-scheelite

transformation, which is claimed to be the result of simple shearing of zircon structure followed by small atomic adjustments [52]. As a consequence, the high pressure scheelite phase should inherit the lattice strain of the zircon phase during phase transformation, hence the high initial *t/G* value for the scheelite phase that is measured at the beginning of the phase transformation.

The high differential stress under non-hydrostatic pressure can produce plastic deformation and this behavior is investigated by the texture analysis. Upon compression, the zircon-type $GdVO_4$ develops a texture characterized by a maximum along the 001 direction and minima along 010 and 110 directions in the inverse pole figures, as seen in Fig.3. The intensity of the 001 texture increases with the initial compression. It then decreases during the phase transformation to the scheelite phase. The appearance and increase of texture strength in the initial compression stage is induced by the plastic deformation of zircon $GdVO_4$ under pressure. After the zircon-scheelite phase transition, the scheelite phase readily shows a texture with a maximum at 110 and minima at 001 and 010. The texture becomes stronger with pressure while the volume ratio increases. At 23 GPa, the zircon phase completely disappears while the scheelite phase shows a remarkable texture with a maximum pole density of 7.11 at 110.

The development of textures depends on the deformation geometry and the relative activities of slip systems. In order to infer the active slip systems in the zircon phase under high pressure, we compare the experimental textures with those generated from polycrystal plasticity. For these simulations we used the Los Alamos visco-plastic self-consistent code (VPSC), which treats each grain as an inclusion in a homogeneous but anisotropic matrix that has the average properties of the polycrystal. As deformation

proceeds, crystals deform and rotate to generate preferred orientation. By applying different critical resolved shear stresses (CRSSs) to slip systems, the model will favor one deformation mode over another. This results in different textures for different combinations of deformation models. By determining which simulated texture most closely resembles the experimental texture, we can infer which slip systems are active under the experimental conditions. By applying different CRSSs to various slip systems 7 different models were generated to find a best match to the experiment result. Parameters used for each model are shown in Table 1. Some example slip systems are showing in Fig. 4 (a). For each model, we start with a randomly oriented sample of 3000 grains. We deform the sample incrementally in 100 steps to a total of 50% strain to match the intensity of the textures observed experimentally. Results of the modeling are displayed in Fig.4. It can be clearly seen that model 2 provides textures that best agree with the experimental results. In this case, deformation is strongly dominated by the <100>{001}slip system (54% of the total plastic activity), while the slip system <100>(010) shows a plastic activity of 16%. The rest of the deformation is accommodated by <11-1>{112} slip (30%). The agreement between experimental textures and simulated textures could not be improved with other slip systems combinations.

The zircon to scheelite phase transformation has been investigated using TEM on quenched shock deformed samples [25]. Leroux *et al.* found that the scheelite phase was in a close epitaxial relationship with zircon, with $\{100\}_z$ // $\{112\}_s$ and $[001]_z$ // $<110>_s$. This conclusion is consistent with the result reported by Kusaba *et al.* on the shock-induced zircon to scheelite transformation, in which the [110] direction in zircon was

observed to become the [001] direction in the scheelite [52]. It is also consistent with observations in natural samples [6]. In our work, the zircon-type $GdVO_4$ shows a (001) texture while the scheelite phase shows a (110) texture, which agrees well with the above relationship. The (110) texture of scheelite is hence inherited from the (001) texture of the zircon phase. The observed textures in the scheelite phase do not evolve upon further compression. Therefore, it can be concluded that the measured textures in the scheelite phase are mainly inherited from that of the zircon phase during the phase transformation, with little contribution from the further plastic deformation in the experiment.

In our work, the texture evolution of zircon-type $GdVO_4$ under plastic deformation and through phase transition was systematically investigated via radial x-ray diffraction in a diamond anvil cell. In the low pressure zircon phase, we observe preferential alignment of (001) poles with the compression direction. This is attributed to dominant slip on <100>{001}, combined with two other slip systems, <100>(010) and <11-1>{112}. Due to the topotactic relationship $[001]_z$ // $<110>_s$ during the phase transformation, the high pressure scheelite phase inherits the texture from the previous zircon phase and develops a texture with a maximum at 110. The present work contributes to achieve a deeper understanding of the plastic deformation of zircon-type oxides which are both of technological and geophysical importance. It is also an important contribution towards the understanding of pressure-induced martensitic transformations, which could be useful for the development of new shape memory materials.

The authors would like to thank Hugues Leroux and Nadège Hilairet for fruitful discussions and Prof. Zhenxiang Cheng for providing the sample. The authors

acknowledge the support of NSAF (Grant No: U1530402). The Advanced Light Source is supported by the Director, Office of Science, Office of Basic Energy Sciences, of the U.S. Department of Energy under Contract No. DE-AC02-05CH11231. Part of work is supported by COMPRES (the Consortium for Materials Properties Research in Earth Sciences) under NSF Cooperative Agreement EAR 10-43050. S.M. is supported by the Institut Universitaire de France.

References

[1] R. J. Finch and J. M. Hanchar, Rev. Mineral. Geochem. **53**, 1 (2003).

[2] P. Glass Billy, S. Liu, and B. Leavens Peter, Am. Mineral. **87**, 562 (2002).

[3] S. A. Wilde, J. W. Valley, W. H. Peck, and C. M. Graham, Nature **409**, 175 (2001).

[4] J. W. Valley *et al.*, Nature Geosci. **7**, 219 (2014).

[5] E. Kovaleva, U. Klötzli, G. Habler, and E. Libowitzky, Solid Earth Discuss. **6**, 1799 (2014).

[6] A. J. Cavosie, T. M. Erickson, and N. E. Timms, Geology **43**, 315 (2015).

[7] E. Danielson, J. H. Golden, E. W. McFarland, C. M. Reaves, W. H. Weinberg, and X. D. Wu, Nature **389**, 944 (1997).

[8] T. V. Gavrilović, D. J. Jovanović, V. Lojpur, and M. D. Dramićanin, Sci. Rep. **4**, 4209 (2014).

[9] X. Huang, S. Han, W. Huang, and X. Liu, Chem. Soc. Rev. **42**, 173 (2013).

[10] S. R. Choubey, S. C. Gedam, and S. J. Dhoble, Radiat. Eff. Defects Solids **170**, 7 (2015).

[11] D. Errandonea and F. J. Manjón, Prog. Mater. Sci. **53**, 711 (2008).

[12] D. Errandonea, R. S. Kumar, S. N. Achary, and A. K. Tyagi, Phys. Rev. B **84**, 224121 (2011).

[13] D. Errandonea, C. Popescu, S. N. Achary, A. K. Tyagi, and M. Bettinelli, Mater. Res. Bull. **50**, 279 (2014).

[14] X. Wang, I. Loa, K. Syassen, M. Hanfland, and B. Ferrand, Phys. Rev. B **70**, 064109 (2004).

[15] D. Errandonea, R. Lacomba-Perales, J. Ruiz-Fuertes, A. Segura, S. N. Achary, and A. K. Tyagi, Phys. Rev. B **79**, 184104 (2009).

[16] A. B. Garg and D. Errandonea, J. Solid State Chem. **226**, 147 (2015).

[17] C. C. Zhang, Z. M. Zhang, R. C. Dai, Z. P. Wang, J. W. Zhang, and Z. J. Ding, J. Phys. Chem. C **114**, 18279 (2010).

[18] W. Paszkowicz *et al.*, J. Phys.: Condens. Matter **26**, 025401 (2014).

[19] Z. Huang, L. Zhang, and W. Pan, J. Solid State Chem. **205**, 97 (2013).

[20] B. G. Alka, D. Errandonea, P. Rodríguez-Hernández, S. López-Moreno, A. Muñoz, and C. Popescu, J. Phys.: Condens. Matter **26**, 265402 (2014).

[21] C. Popescu, B. G. Alka, D. Errandonea, J. A. Sans, P. Rodriguez-Hernández, S. Radescu, A. Muñoz, S. N. Achary, and A. K. Tyagi, J. Phys.: Condens. Matter **28**, 035402 (2016).

[22] K. Otsuka and X. Ren, Prog. Mater. Sci. **50**, 511 (2005).

[23] T. Krenke, E. Duman, M. Acet, E. F. Wassermann, X. Moya, L. Manosa, and A. Planes, Nat. Mater. **4**, 450 (2005).

[24] D. E. Eakins, J. B. LeBret, M. G. Norton, and D. F. Bahr, J. Cryst. Growth **266**, 411 (2004).

[25] H. Leroux, W. U. Reimold, C. Koeberl, U. Hornemann, and J. C. Doukhan, Earth Planet. Sci. Lett. **169**, 291 (1999).

[26] S. Piazolo, H. Austrheim, and M. Whitehouse, Am. Mineral. **97**, 1544 (2012).

[27] S. Reddy, N. Timms, W. Pantleon, and P. Trimby, Contrib. Mineral. Petrol. **153**, 625 (2007).

[28] S. Merkel, A. K. McNamara, A. Kubo, S. Speziale, L. Miyagi, Y. Meng, T. S. Duffy, and H.-R. Wenk, Science **316**, 1729 (2007).

[29] H. Marquardt and L. Miyagi, Nature Geosci. **8**, 311 (2015).

[30] S. Merkel, H. P. Liermann, L. Miyagi, and H. R. Wenk, Acta Mater. **61**, 5144 (2013).

[31] L. Miyagi, W. Kanitpanyacharoen, P. Kaercher, K. K. M. Lee, and H.-R. Wenk, Science **329**, 1639 (2010).

[32] H. R. Wenk, P. Kaercher, W. Kanitpanyacharoen, E. Zepeda-Alarcon, and Y. Wang, Phys. Rev. Lett. **111**, 195701 (2013).

[33] S. Merkel and T. Yagi, Rev. Sci. Instrum. **76**, 046109 (2005).

[34] V. N. Antonov, V. Y. Milman, V. V. Nemoshkalenko, and A. V. Zhalko-Titarenko, Z. Phys. B: Condens. Matter **79**, 233 (1990).

[35] H. M. Rietveld, J. Appl. Crystallogr. **2**, 65 (1969).

[36] L. Lutterotti, S. Matthies, H.-R. Wenk, A. S. Schultz, and J. W. Richardson, J. Appl. Phys. **81**, 594 (1997).

[37] M. Marqués, M. Flórez, J. M. Recio, L. Gerward, and J. S. Olsen, Phys. Rev. B **74**, 014104 (2006).

[38] O. Tschauner, S. V. Ushakov, A. Navrotsky, and L. A. Boatner, J. Phys.:

Condens. Matter **28**, 035403 (2016).

[39] See Supplemental Material at [URL] for texture refinement, EOS and data analysis details, which includes Refs. [12, 14, 16, 20, 21, 35, 36, 40-46]

[40] Z. Huang, L. Zhang, J. Feng, X. Cui, and W. Pan, J. Alloys Compd. **538**, 56 (2012).

[41] Z. Huang, L. Zhang, and W. Pan, Inorg. Chem. **51**, 11235 (2012).

[42] R. J. Angel, J. Gonzalez-Platas, and M. Alvaro, Z. Kristallogr. **229**, 405 (2014).

[43] O. Gomis, J. A. Sans, R. Lacomba-Perales, D. Errandonea, Y. Meng, J. C. Chervin, and A. Polian, Phys. Rev. B **86**, 054121 (2012).

[44] A. P. Hammersley, S. O. Svensson, M. Hanfland, A. N. Fitch, and D. Hausermann, High Pressure Res. **14**, 235 (1996).

[45] N. C. Popa and D. Balzar, J. Appl. Crystallogr. **35**, 338 (2002).

[46] S. Matthies and G. W. Vinel, Phys. Status Solidi B **112**, K111 (1982).

[47] D. Errandonea, Y. Meng, M. Somayazulu, and D. Häusermann, Physica B **355**, 116 (2005).

[48] R. Lacomba-Perales *et al.*, Phys. Rev. B **81**, 144117 (2010).

[49] A. K. Singh, C. Balasingh, H.-k. Mao, R. J. Hemley, and J. Shu, J. Appl. Phys. **83**, 7567 (1998).

[50] S. Merkel, C. Tomé, and H. R. Wenk, Phys. Rev. B **79**, 064110 (2009).

[51] P. Raterron, S. Merkel, and C. W. Holyoke, Rev. Sci. Instrum. **84**, 043906 (2013).

[52] K. Kusaba, T. Yagi, M. Kikuchi, and Y. Syono, J. Phys. Chem. Solids **47**, 675 (1986).

Captions:

Figure 1. Crystal structures and fitting example of $GdVO_4$. (a) Zircon, (b) scheelite and (**c**) *M*-fergusonite phase. The zircon phase begins to transform to a scheelite phase below 5 GPa. The transition is complete at 23 GPa. A subsequent transformation to a *M*-fergusonite phase occurs at 31 GPa. (d) Fitting example at 11 GPa. The bottom half of the pattern is the experimental data and the top is the calculated pattern from the Rietveld refinement. Chi square (χ^2) is 1.071. Some diffraction lines from zircon and scheelite phases are labeled ("z" for zircon, "s" for scheelite). Others are not due to multiple peak overlaps between the two phases. Green arrows indicate the compression direction.

Figure 2. Refinement results for $GdVO_4$ under pressure. (a) Volume fraction, (b) unit cell parameters, (c) unit-cell volume (dashed lines are EOS fitting results), and (d) *t/G* ratio of zircon and scheelite phases as a function of pressure. The average values of *t/G* shown in (d) are weighted means of those measured in both phases, *t* is the differential stress and *G* is the shear modulus. For the *M*-fergusonite phase, only the volume fraction is shown.

Figure 3. Texture evolution of $GdVO_4$ through the phase transition. Invers pole figures of the compression direction are shown up to 23 GPa for both zircon and scheelite phase. For each case, the experimental pressure and phase proportions are shown in the figure. Pole densities are measured in multiples of a random distribution (mrd). Equal area projections.

Figure 4. Dominate slip systems for zircon phase under plastic deformation. (a) Slip systems reported in literatures. (b) Inverse pole figures calculated from seven VPSC models. The corresponding slip systems activities for each model are shown in Table 1. Pole densities in mrd. Equal area projections.

Figure 1

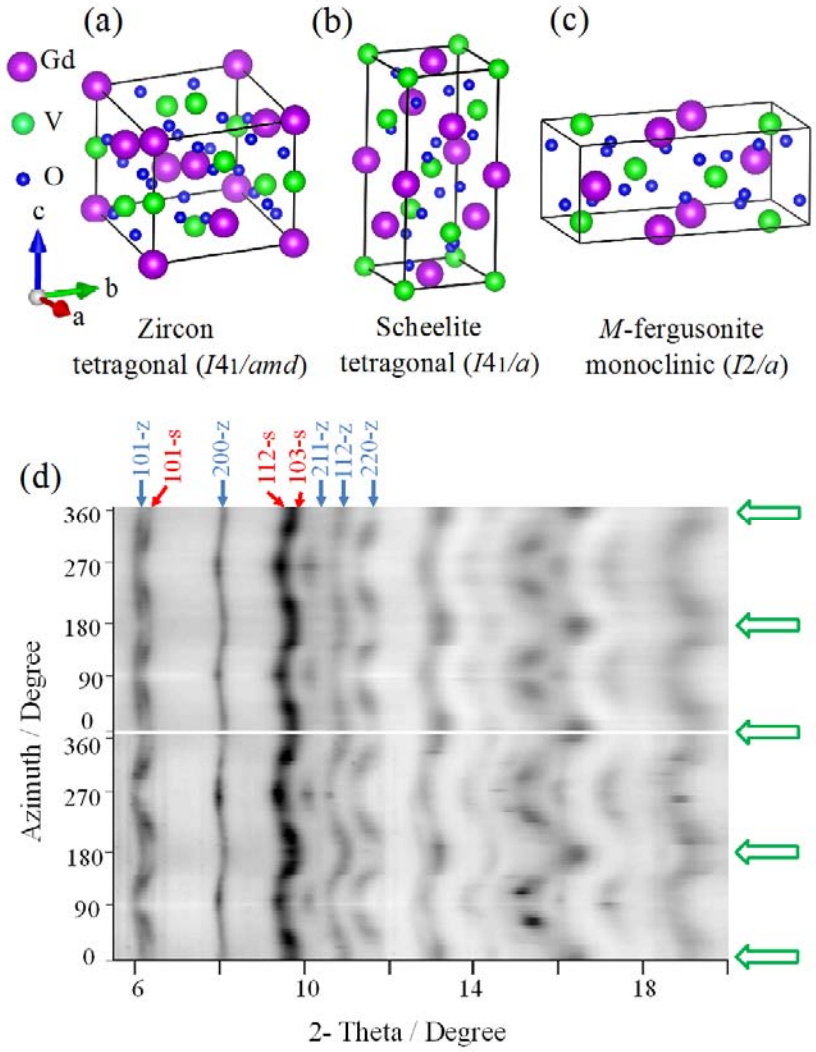
(a)
(b)
(c)
Gd
V
O
c
b
a
Zircon
tetragonal (I41/amd)
Scheelite
tetragonal (I41/a)
M-fergusonite
monoclinic (I2/a)
(d)
101-z
101-s
200-z
112-s
103-s
211-z
112-z
220-z
360
270
180
90
0
Azimuth / Degree
6
10
14
18
2- Theta / Degree

Figure 2

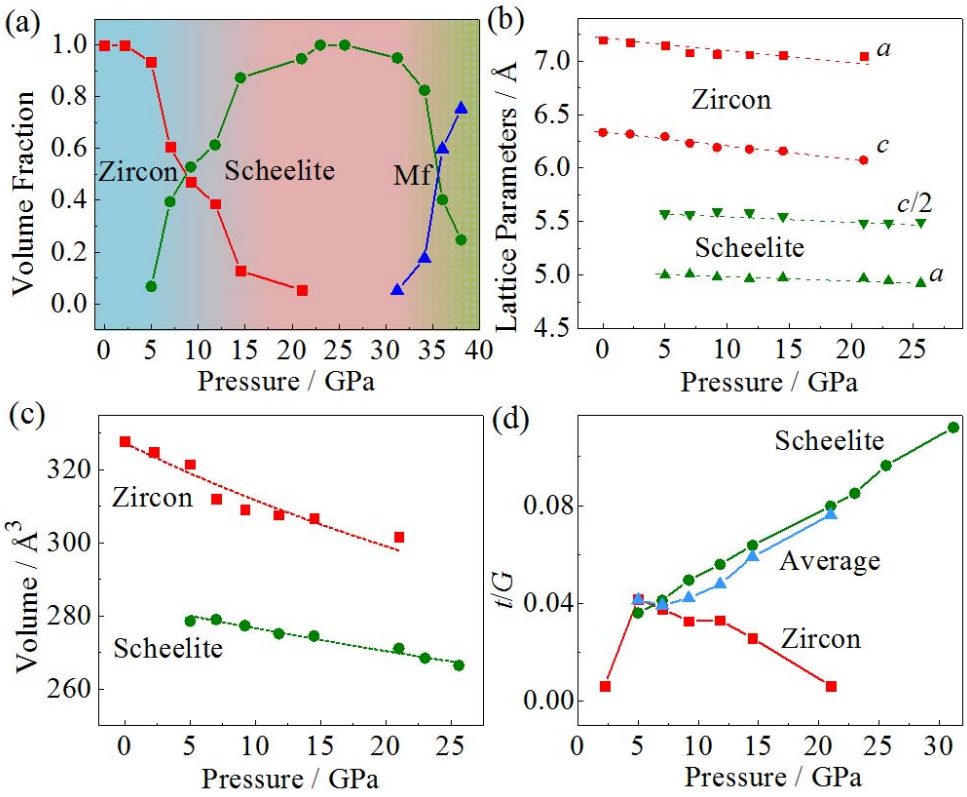
(a)
Volume Fraction
Zircon
Scheelite
Mf
Pressure / GPa
(b)
Lattice Parameters / Å
Zircon
a
c
c/2
Scheelite
a
Pressure / GPa
(c)
Volume / Å3
Zircon
Scheelite
Pressure / GPa
(d)
t/G
Scheelite
Average
Zircon
Pressure / GPa

Figure 3

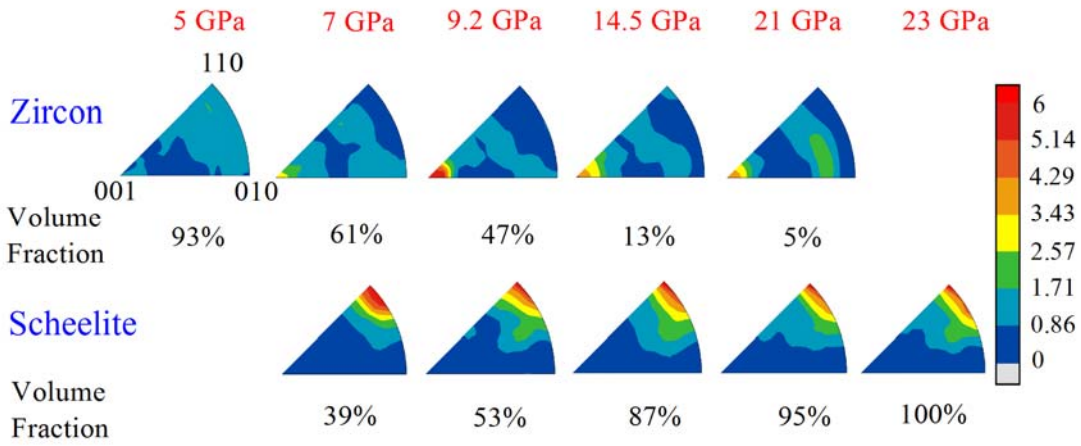
5 GPa
7 GPa
9.2 GPa
14.5 GPa
21 GPa
23 GPa
110
Zircon
001
010
Volume Fraction
93%
61%
47%
13%
5%
Scheelite
Volume Fraction
39%
53%
87%
95%
100%
6
5.14
4.29
3.43
2.57
1.71
0.86
0

Figure 4

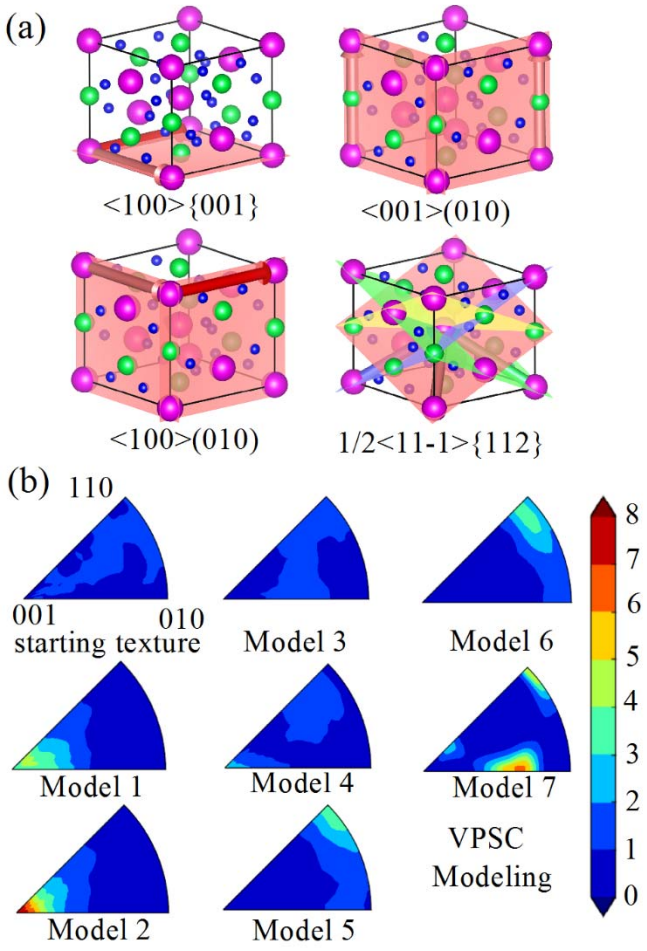
(a)
<100>{001}
<001>(010)
<100>(010)
1/2<11-1>{112}
(b)
110
001
010
starting texture
Model 3
Model 6
Model 1
Model 4
Model 7
VPSC
Modeling
Model 2
Model 5
8
7
6
5
4
3
2
1
0

Table 1. VPSC calculation parameters. Each line is a simulation with a different dominant slip system. For each, we report the CRSS (Critical resolved shear stresses) of each slip system and their relative plastic activity (Act., in percent). The corresponding compression textures are shown in Fig. 4 (b).

	<100>{001}		**<110>{001}**		**<100>(010)**		**[001](010)**		**<1-10>{111}**		**<11-1>{112}**	
	CRSS	Act.	CRSS	Act.	CRSS	Act.	CRSS	Act.	CRSS	Act.	CRSS	Act.
Model 1	0.5	57%	*	0%	1	16%	1	0%	10	27%	*	0%
Model 2	0.5	54%	*	0%	1	16%	1	0%	100	0%	10	30%
Model 3	1	25%	*	0%	0.5	27%	1	25%	10	23%	*	0%
Model 4	1	27%	*	0%	0.5	29%	1	27%	100	0%	10	17%
Model 5	1	0%	*	0%	1	35%	0.5	41%	10	24%	*	0%
Model 6	1	0%	*	0%	1	41%	0.5	45%	100	0%	10	13%
Model 7	*	0%	0.1	0%	1	5%	1	10%	100	85%	10	0%